ACS APPLIED MATERIALS & INTERFACES

www.acsami.org

Research Article

4D Printing of a Light-Driven Soft Actuator with Programmed Printing Density

Akihiro Nishiguchi, Hang Zhang, Sjören Schweizerhof, Marie Friederike Schulte, Ahmed Mourran, and Martin Möller*

Cite This: *ACS Appl. Mater. Interfaces* 2020, 12, 12176–12185

Read Online

ACCESS | Metrics & More | Article Recommendations | Supporting Information

ABSTRACT: There is a growing interest in the concept of four-dimensional (4D) printing that combines a three-dimensional (3D) manufacturing process with dynamic modulation for bioinspired soft materials exhibiting more complex functionality. However, conventional approaches have drawbacks of low resolution, control of internal micro/nanostructure, and creation of fast, complex actuation due to a lack of high-resolution fabrication technology and suitable photoresist for soft materials. Here, we report an approach of 4D printing that develops a bioinspired soft actuator with a defined 3D geometry and programmed printing density. Multiphoton lithography (MPL) allows for controlling printing density in gels at pixel-by-pixel with a resolution of a few hundreds of nanometers, which tune swelling behaviors of gels in response to external stimuli. We printed a 3D soft actuator composed of thermoresponsive poly(*N*-isopropylacrylamide) (PNIPAm) and gold nanorods (AuNRs). To improve the resolution of printing, we synthesized a functional, thermoresponsive macrocrosslinker. Through plasmonic heating by AuNRs, nanocomposite-based soft actuators undergo nonequilibrium, programmed, and fast actuation. Light-mediated manufacture and manipulation (MPL and photothermal effect) offer the feasibility of 4D printing toward adaptive bioinspired soft materials.

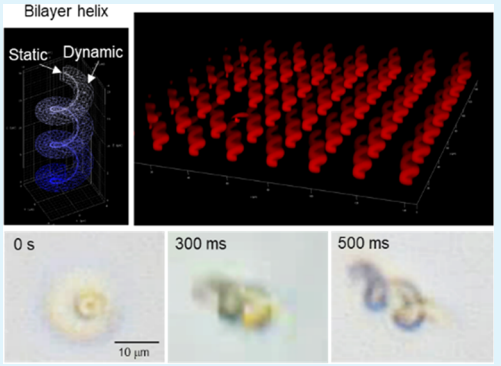

KEYWORDS: *optically active materials, multiphoton lithography, hydrogels, composite materials, gold nanorods*

INTRODUCTION

Microstructural anisotropy in living organisms is of great importance for an autonomous, dynamic actuation such as bending of plants, ciliary motion, and muscle contraction.[1] Hierarchically ordered fibrous, layered, cellular, gradient, and helical structures regulate their actuation in response to external stimuli. For example, pine cones show hydration-triggered opening and closing by anisotropic multilayers where local stress is generated by constrained volume change.[2] At the molecular level, collagen forms an assembled helical architecture that may provide increased strength and toughness in multiple dimensions.[1] There have been growing interests in autonomous, self-regulating soft actuators[3−6] inspired by biological systems for a wide range of applications like shape memory,[7] reactors,[8] soft robots,[9] and microswimmers.[10] Especially, a hydrogel is a prominent example of an adaptive soft material that can change its swelling behavior and the volume in response to external stimuli (pH, ionic strength, temperature, and light).[11] The swelling degree of hydrogels depends on the internal structures including crosslinking density, microstructural anisotropy, and hydrophilicity. Therefore, an anisotropic bilayer structure possessing different internal structures causes stress and results in large amplitude bending, folding, and buckling, although a homogeneously crosslinked gel displays isotropic volume change. Despite much effort to design controlled actuation by tuning the internal structure of hydrogels using two-dimensional (2D) soft lithography,[12−16] none of them is single step and can be used to fabricate three-dimensional (3D) structures with control over micro- or nanoscale features, which is necessary for replicating a rapid, nastic motion in nature such as mimosa, the Venus flytrap, and seed and pollen dispersal.[17] It would be expected that further geometrical control in all three dimensions realizes the control of complex actuation and micro/nanofabrication of gels provides fast actuation through uptake and release of water in a short time. An approach enabling these requirements leads to bioinspired applications of soft microrobots, actuators, and devices for mixing, sorting, and circulating fluids.

The concept of four-dimensional (4D) printing that combines a 3D manufacturing process with dynamic modulation of materials may offer the feasibility for the next generation of bioinspired materials that exhibit more complex

Received: February 13, 2020
Accepted: February 19, 2020
Published: February 19, 2020

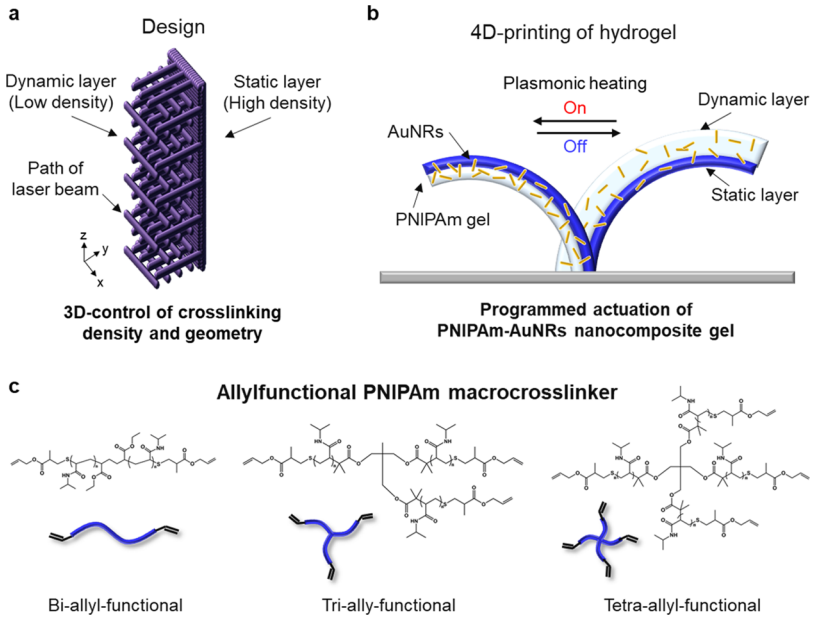

Figure 1. Schematic illustration of 4D printing of the hydrogel. (a) CAD design of hydrogel structure. The pillar structure comprised dynamic and static layers that possessed low and high printing density and distinct thickness. (b) Schematic illustration of 3D printing of PNIPAm−AuNR nanocomposite gel and light-induced actuation through plasmonic heating of AuNRs. The actuation of gels can be programmed by the design. (c) Chemical structure of multiarmed ally-functional PNIPAm macrocrosslinker including bi-, tri-, and tetra-allyl-functional PNIPAm.

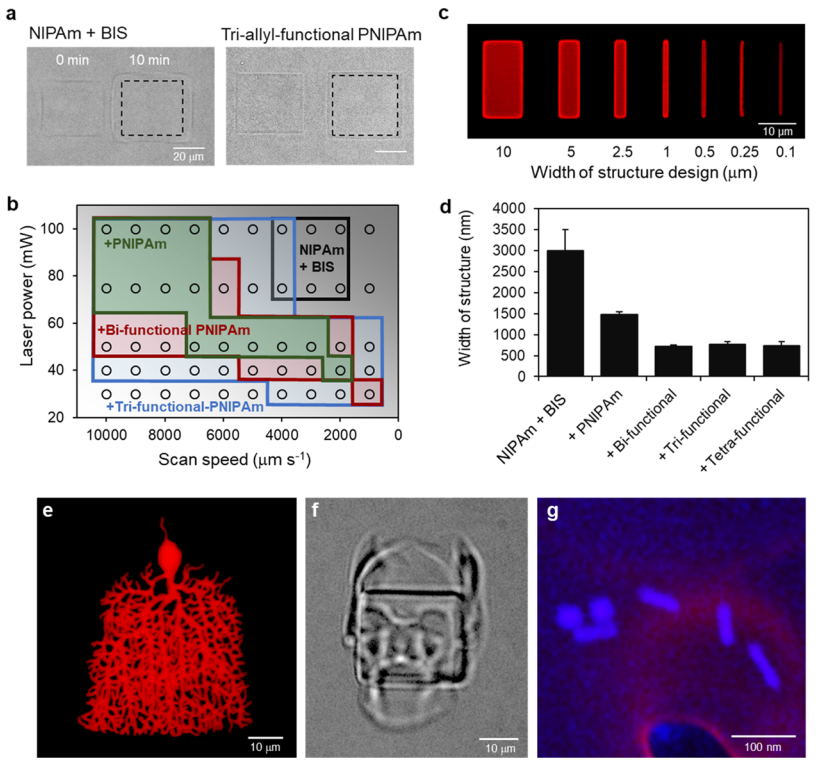

Figure 2. Development of gel photoresist and 3D printing by MPL. (a) Phase-contrast images of PNIPAm gels prepared using photoresists without and with tri-allyl-functional PNIPAm macrocrosslinkers soon after writing and after 10 min. Black dashes denote the size of the original design. (b) Gelation diagram of each gel photoresist. Different laser powers and scanning speeds ranging from 30 to 100 mW and 1000 to 10 000 mm/s, respectively, were applied to gel photoresists composed of NIPAm + Bis with or without PNIPAm, bi-, and trifunctional PNIPAm macrocrosslinkers. (c, d) Writing resolution of the gel photoresist. (c) CLSM image of the cuboids with 30 μm in length, 1 μm in height, and different widths ranging from 10 to 0.1 μm in design using the gel photoresist with tri-allyl-functional PNIPAm macrocrosslinkers. (d) Width of these structures printed using gel photoresists composed of NIPAm + Bis with and without additional crosslinkers or additives (plane PNIPAm, bi-, and trifunctional PNIPAm macrocrosslinkers) was measured. The smallest width was defined as the resolution (n = 3). (e) CLSM image of the neuronlike branched, complex gel structure. (f) Phase-contrast image of the skull-like 3D structure. (g) Elemental mapping of AuNRs (blue, AR = 4.4) embedded within the PNIPAm gel (red) by FESEM observation.

https://dx.doi.org/10.1021/acsami.0c02781
ACS Appl. Mater. Interfaces 2020, 12, 12176−12185

functionality.[18−20] Multiphoton lithography (MPL), which is also known as direct laser writing, substantially improves the fabrication process of 3D micro/nanostructures in 4D printing.[21,22] Due to the nonlinearity of the multiphoton absorption process, the polymerization/crosslinking of a photoresist is confined at a focal point, leading to high spatial resolution (~200 nm). Although MPL has been commonly used for rigid materials with acrylic and epoxy resin,[23] much less attention has been paid to soft materials despite their promising applications. This high-resolution 3D printing approach has been applied for the micro/nanofabrication of hydrogels.[24−28] However, these methods have crucial problems of low resolution, control of internal micro/nanostructure, and creation of fast, complex actuation. Therefore, 4D printing of stimuli-responsive hydrogels for biomimetic materials should be addressed and the relationship between internal material distribution and their actuation needs to be investigated.

Here, we report an approach of 4D printing that develops a bioinspired soft actuator with a defined 3D geometry and programmed density of the printed network (printing density) by the MPL technique (Figure 1). A one-step fabrication process using MPL allows for controlling the material density in gels pixel-by-pixel with a resolution of a few hundreds of nanometers, while the crosslinking density at the molecular level is almost the same in each line of writing. Writing distance between each line was programmed using computer-aided design (CAD). This programmed writing distance determines the printing density in gels and tunes the swelling property of gels. A small distance between each line of focal point results in high printing density and the formation of a static gel layer (Figure 1a). Since only low printing density of the dynamic layer can actuate in response to external stimuli, a bilayer pillar with distinct printing density shows an anisotropic, programmed actuation. Recently, we reported that a thermoresponsive, PNIPAm gel embedded with AuNRs can provide ultrafast, repetitive actuation based on body shape deformation through plasmonic heating.[10] Due to the light-effectuated thermal response, nanocomposite gels undergo nonequilibrium actuation comprising a distinct forward and reverse stroke, which is an essential property to move at low Reynolds numbers ($Re < 1$), leading to an artificial microswimmer. Based on this knowledge, we printed a 3D nanocomposite of PNIPAm and size-defined AuNRs allowing for remotely controlled energy uptake (Figure 1b). To improve the resolution of printing, we synthesized a newly multiarmed, thermoresponsive macrocrosslinker of PNIPAm (Figure 1c). Light-mediated manufacture and manipulation (MPL and photothermal effect)[29] offer the feasibility of 4D printing toward adaptive bioinspired soft materials.

RESULTS AND DISCUSSION

Gel Photoresist for 3D Printing. A thermoresponsive PNIPAm gel was printed using a gel photoresist by an MPL system. Due to lower critical solution temperature (LCST, around 32 °C),[30] the PNIPAm hydrogel reveals a sharp, reversible volume transition in response to temperature. The NIPAm monomer, *N*,*N*′-methylenebis-acrylamide (Bis), and a photoinitiator (Irgacure 819, Ex ≈ 400 nm) were dissolved in an ethylene glycol/acetone solution to prepare a gel photoresist. The gel photoresist on a coverslip was placed on the stage of MPL with a femtosecond laser, a 3D piezo scanning stage, and an oil immersion 63× objective lens (NA = 1.4). Tightly focused laser beam at focal points induced photopolymerization/crosslinking to form PNIPAm gels. Although PNIPAm gels were printed using a photoresist comprising of a NIPAm monomer and Bis, swelling of gels occurred during writing, which decreased the resolution (Figure 2a). To enhance the resolution, we newly synthesized bi-, tri-, and tetra-allyl-functional PNIPAm macrocrosslinkers by reversible addition−fragmentation chain transfer (RAFT) polymerization followed by a one-pot double modification using octylamine and allyl methacrylate as reactants (Figures S1−S10 and Table S1). Each macrocrosslinker was composed of PNIPAm as the main chain and a terminating crosslinkable allyl group. Compared to Bis, multiarmed macrocrosslinkers may promote the efficiency of the gelation reaction because of their higher viscosity, molecular weight, and the number of double bonds as a crosslinking point, which contributes to diffusion-controlled propagation and reaction diffusion-controlled termination in gelation kinetics,[31] especially for the MPL system. As shown in Figure 2a, the photoresist with a tri-allyl-functional macrocrosslinker suppressed the swelling of gels even after 10 min of writing. The efficiency of gelation of each photoresist was evaluated using different photoresists: NIPAm and Bis (NIPAm + Bis); NIPAm + Bis with bi-, tri-, and tetra-allyl-functional PNIPAm macrocrosslinkers; and NIPAm + Bis with PNIPAm without allyl groups (Figures 2b and S11). The efficiency of gelation was defined by the dose of writing conditions, which is the combination of laser power and scanning speed. While the photoresist of NIPAm + Bis required a high dose of writing conditions (high laser power and slow scanning speed), the photoresist of multiarmed bi-allyl-functional and tri-allyl-functional PNIPAm macrocrosslinkers formed gels with lower laser power and fast scanning speed by promoting the crosslinking reaction via ally groups of macrocrosslinkers. Multiarmed PNIPAm macrocrosslinkers increased the viscosity of photoresists up to 180 MPa·s (Table S2), which contributes to polymerization efficiency because photopolymerization proceeds in focal volume only, and low diffusion coefficient is preferable. The tetra-allyl-functional PNIPAm macrocrosslinker was not completely dissolved in ethylene glycol/acetone and did not promote gelation efficacy. Although PNIPAm without allyl groups enhanced the efficiency of gelation by increasing the viscosity of the photoresist, it required higher dose as compared to multiarmed allyl-functional PNIPAm, indicating the importance of allyl groups as a crosslinking point. Among macrocrosslinkers, the tri-allyl-functional macrocrosslinker shows superior usability because the bi-allyl-functional macrocrosslinker has less crosslinking points in terms of arm number and the tetrafunctional macrocrosslinker shows poor solubility in the solvent. Moreover, the tri-allyl-functional PNIPAm macrocrosslinker showed the largest range of printing dose and did not cause bubbles at high laser intensity unlike other photoresists, which is useful to create tall 3D structures requiring high laser intensity. We also evaluated the resolution of printing using each gel photoresist by measuring the width of printed lines (original design of structures: 30 μm in length; 0.1, 0.25, 0.5, 1, 2.5 5, or 10 μm in width; and 1 μm in height) with confocal laser scanning microscopy (CLSM) (Figure 2c). Since the lateral and axial radii of the focal points are approximately 150 and 300 nm, respectively, the smallest width of structure design was set to 100 nm. After printing and swelling in water, the smallest width of the gel printed using each different photoresist was measured. As a result, the resolution of gels was approximately 760 nm when tri-allyl-

https://dx.doi.org/10.1021/acsami.0c02781
ACS Appl. Mater. Interfaces 2020, 12, 12176−12185

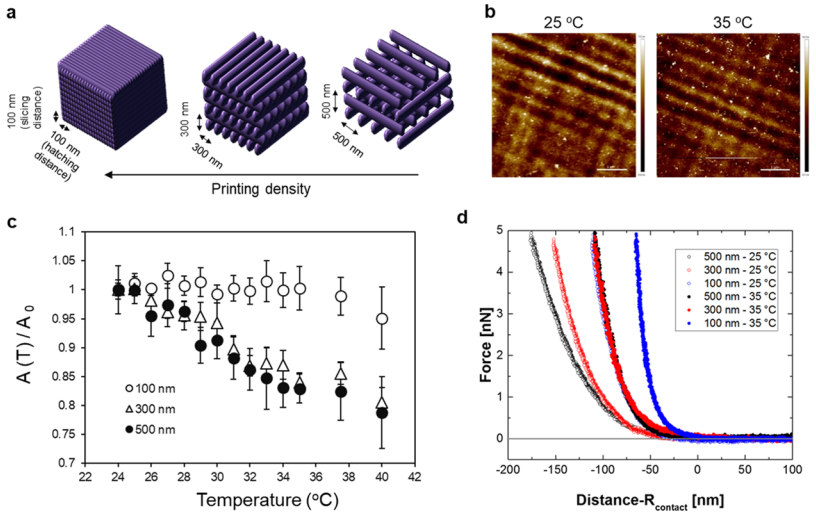

Figure 3. Relationship between programmed printing density and structural properties. (a) Schematic illustration of internal structures of gels with designed printing density. The hatching/slicing distance was varied in a range of 100, 300, and 500 nm to tune the printing density. (b) Height image of the surface of hydrated gels with the 100 nm hatching/slicing distance at 25 and 35 °C. (c) Swelling/deswelling behavior of the PNIPAm gel with 100, 300, and 500 nm of hatching/slicing distances at different temperature. The gels were harvested in water by treatment with HF. The area of gels at a certain temperature ($A(T)$) was measured from the phase-contrast images (n = 10). A_0 denotes the area of gels at 24 °C. (d) Force−distance curve corrected by the contact point for the vertical approach of a colloidal AFM tip toward the solid substrate on three different hydrated gels: 100 nm (blue), 300 nm (red), and 500 nm (black) at T = 25 °C (open symbols) and T = 35 °C (filled symbols).

functional macrocrosslinkers were used, which is more than 4 times better than that of the NIPAm + Bis (Figure 2d). These results indicated that the multiarmed allyl-functional PNIPAm macrocrosslinker can suppress swelling of gels and improve the resolution of printing. Based on these results, the gel photoresist composed of trifunctional PNIPAm was employed in the following experiments. Using this photoresist, 3D complex structures including a neuronlike branched network structure and a skull-like 3D structure were printed at the submicrometer scale (Figure 2e,f).

Ultrafast actuation of gels can be achieved by very fast temperature jump localized to the volume of gels through plasmonic heating of AuNRs. AuNRs convert light energy into heat so that the temperature of the gel can increase by more than 20 °C within milliseconds[10] to induce the volume phase transition of PNIPAm gels. Moreover, the hydrogel object also cools down fast because of the confined heating in the inner volume of the small microgel and fast heat transfer to the surrounding water. This ultrafast cyclic temperature jumps effectuate nonequilibrium actuation with distinct forward and backward paths in the volume/shape because diffusion-controlled swelling/deswelling cannot follow the jump in time. To prepare a nanocomposite gel of PNIPAm−AuNRs, AuNRs with aspect ratios (ARs) of 2.5 and 4.4, whose longitudinal plasmon absorption were 620 and 810 nm of light, respectively, were incorporated within the PNIPAm gel (Figure S12). By changing the AR of AuNRs, the absorption wavelength can be tuned. These AuNRs were dispersed in a photoresist with a number density of 0.38 particles per μm^3, which was estimated by UV−vis spectroscopy, corresponding to a volume fraction of <0.001%. The AuNRs were fully modified with a high molecular weight of thio-functional PNIPAm (PNIPAm-SH, 45 kDa) to be stabilized in ethylene glycol. A gel photoresist containing AuNRs with ARs of 2.5 and 4.4 successfully provided nanocomposite gels, although the AR 4.4 AuNRs produced bubbles at high laser intensity due to the absorption of the laser beam (λ = 780 nm). Elemental mapping of the cross-sectional nanocomposite gel of AuNRs with AR 4.4 using field-emission scanning electron microscopy (FESEM) revealed that AuNRs were successfully incorporated into the gels (Figure 2g).

Relationship between Programmed Printing Density and Structural Properties. To address whether a programmed printing density can control swelling/deswelling behavior of PNIPAm gels, we printed disk structures (ϕ = 30 μm, h = 5 μm) with different printing densities and measured the changes of top surface area in water when temperature varied. The printing density was encoded by tuning the hatching distance (lateral distance between lines) and slicing distance (vertical distance between layers) in a range of 100, 300, and 500 nm in the original design (Figure 3a). Atomic force microscopy (AFM) observation in water displayed the surface topologies of PNIPAm gels with narrow (100 nm) hatching/slicing distance. A gridlike structure as designed was confirmed, and surface topology became flat due to shrinkage in response to temperature increase to 35 °C (Figure 3b). The increase of hatching/slicing distance results in low printing density, providing a dynamic gel with a large amplitude in response to temperature. The microgel disks were harvested in ultrapure water by etching with hydrogen fluoride (HF), and the diameter was measured at 24−40 °C. Figure 3c shows swelling/deswelling behaviors of gels. PNIPAm gel disks prepared at low printing density with 300 and 500 nm of hatching/slicing distances underwent area change to 0.8 around LCST, indicating the formation of dynamic gels. This is a similar behavior to UV-crosslinked conventional PNIPAm gels, although the extent of volume change was smaller than those. On the other hand, highly crosslinked PNIPAm gels with a 100 nm hatching/slicing distance show no substantial change in the shape and these gels possessed static property. These results indicate that the responsiveness of PNIPAm gels to temperature can be spatially encoded by designed printing density. Moreover, the relationship between printing density and mechanical property of gels was evaluated by force

https://dx.doi.org/10.1021/acsami.0c02781
ACS Appl. Mater. Interfaces 2020, 12, 12176−12185

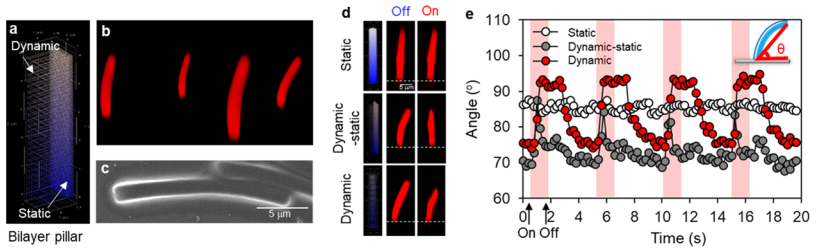

Figure 4. Actuation of bilayer pillar with programmed printing density. (a) CAD image of the bilayer pillar. (b) 3D-reconstructed CLSM image and (c) FESEM image of bilayer pillars. (d) Cross-sectional CLSM images of stiff and soft monolayer pillar and bilayer pillar when the laser was turned on and off. (e) Angle change of three types of pillars as a function of time when the laser was turned on at 1 Hz and off at 0.2 Hz.

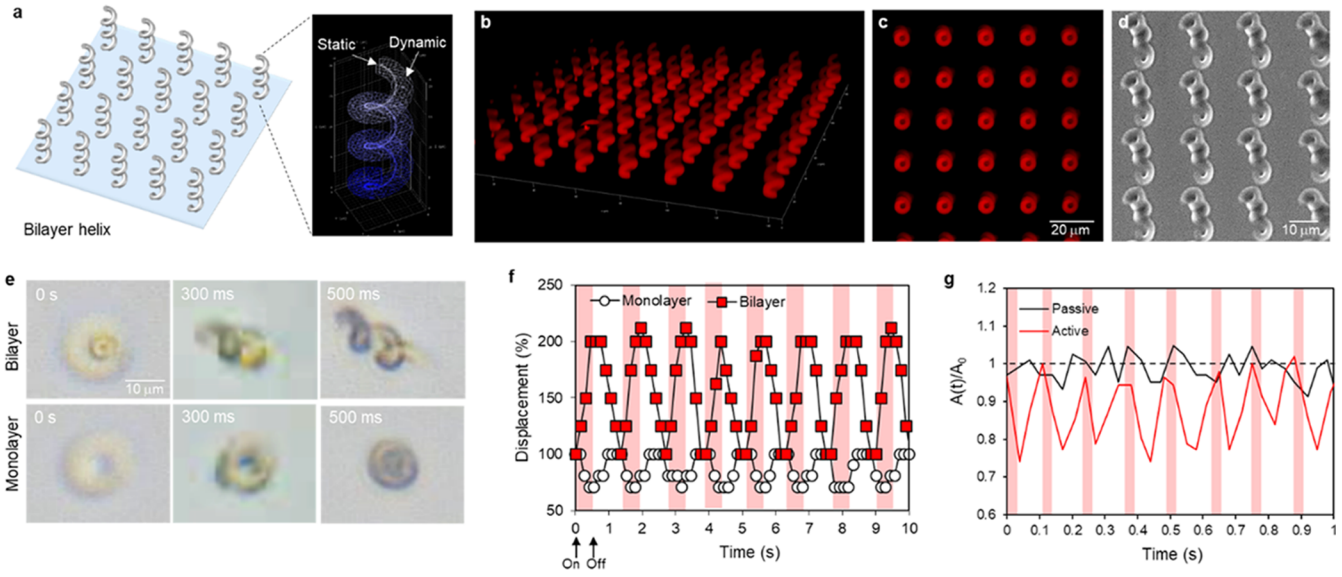

Figure 5. (a) CAD image of the bilayer helix. (b, c) 3D-reconstructed CLSM image and (d) FESEM image of bilayer helices. (e) Phase-contrast images of the bilayer helix and soft monolayer helix after 300 and 500 ms of laser exposure. (f) Displacement of each helix as a function of time when the laser was turned on at 2 Hz and off at 1 Hz. The displacement was defined as follows $(\varepsilon\ (\%) = -(d_0 - d)/d_0 \times 100$, where d_0 is the initial distance from the top edge of the helix to the center of the helix). The cycle of laser exposure was composed of 500 ms turn on and 1 s turn off. (g) Actuation of helices of PNIPAm–AuNR composite gels with 100 (static) and 500 nm (dynamic) of hatching/slicing distances. The cycle of laser exposure was composed of 30 ms turn on and 100 ms turn off. The area of gels at a certain temperature $(A(T))$ was measured from the phase-contrast images. A_0 denotes the area of gels when the laser was turned off.

spectroscopy using AFM. AFM provides nanoscale-resolved mechanical properties, and Young's modulus can be extracted from force spectroscopy measurements.[32−35] Figure 3d exploits the force–distance (z-direction) curve of each PNIPAm gel in water below and above LCST. The force–distance curve was corrected by the contact point for the vertical approach of a colloidal AFM tip toward the solid substrate. At 25 °C, Young's modulus obtained from the curve was 0.088 MPa for 500 nm and 0.22 MPa for 100 nm gel and increased with increasing printing density (Table S4). These measurements indicate that the obtained results on mechanical properties reflect the structural design of gels. Above LCST, Young's modulus increased in all gels due to volume phase transition and these gels show large amplitude of responsiveness in mechanical property against temperature change. The same tendency was also obtained by force spectroscopy using a sharp probe (Figure S13 and Table S5). This result was in good agreement with the result of swelling behavior shown in Figure 3c.

Actuation of the Bilayer Pillar and Helix with Programmed Printing Density. Nature uses an adaptive, complex actuation based on microstructural anisotropy. MPL allows for designing spatial configuration in all dimensions of gels and further developing complex actuation. Figure 4 demonstrates the fabrication of complex structures possessing different printing densities three-dimensionally and their ultrafast actuation using plasmonic heating of AuNRs. As examples, we show bilayer pillars and bilayer helices composed of layers and geometries of distinct printing densities. To confirm the effect of programmed bilayer structure on swelling behaviors, static micropillar (d, 100 nm; ϕ (thickness), 2 μm), static–dynamic micropillar (d, 100 and 500 nm; ϕ, 0.2 and 2 μm), and dynamic micropillar (d, 500 nm; ϕ, 2 μm) were prepared. The 3D-reconstructed CLSM image and FESEM image display that bilayer pillars stand on a substrate in water (Figure 4b) and the structure is homogeneous from top to bottom (Figure 4c). We start with adding AuNRs with an AR of 4.4 into water after printing, which existed surrounding gels, and analyzed their actuation in response to plasmonic heating. The temperature was kept at 20 °C, and 808 nm of stroboscopic illumination was applied to gels. Tuning the length, intensity, and frequency of laser pulses allows for controlling motion sequences. The interval between the illumination was tuned for efficient cooling to visualize large

https://dx.doi.org/10.1021/acsami.0c02781
ACS Appl. Mater. Interfaces 2020, 12, 12176−12185

actuation. Cross-sectional CLSM images show that stiff monolayer pillars did not change their height and angle against a substrate, while soft monolayer pillars shrank in response to plasmonic heating and decrease the height, but there was no change in the angle because of homogeneous monolayer structure (Figure 4d). Bilayer pillars with dynamic and static layers bent before the illumination (curvature, 0.13 μm^{-1} in the bilayer, 0.013 μm^{-1} in static, and 0.047 μm^{-1} in dynamic) and exhibited a sharp transition in volume fast changes of the angle from 75 to 92° in response to local plasmonic heating with AuNRs. The actuation was effectuated within a second via plasmonic heating, and their actuation was remotely controlled and repeatable by stroboscopic illumination (Figure 4e). Additionally, bilayer structures with a certain distance between static layers displayed large amplitude of shape transformation (rolling up below LCST), indicating a high degree of freedom in the design of gel structure and their actuation (Figure S14).

Actuation of the Complex Helical Structure. Moreover, high-resolution 3D printing using the MPL system and newly synthesized gel photoresist enables us to fabricate a core−shell type of bilayer helix that vertically stands on a substrate (Figure 5a). Helices with 8 μm diameter, 20 μm height, and three turns were composed of highly crosslinked static core and dynamic shell whose thicknesses were 200 nm and 2.5 μm in design, respectively. 3D-reconstructed CLSM images show successful printing of helices vertically standing on a glass substrate (Figure 5b,c). Helices possessed homogeneous structures as well as pillars, although they fell down due to drying (Figure 5d). To evaluate the actuation of gels, AuNRs were dispersed in water and the illumination by IR laser was applied. In response to the illumination turned on at 2 Hz and off at 1 Hz off, helical microgels reversibly actuated and fully collapsed within 500 ms (Figure 5e,f). Interestingly, bilayer helices show anisotropic actuation including the twisting and falling motions, while soft monolayer helices actuated isotropically. The difference in responsiveness between static cores and dynamic shells gave rise to internal stress, which led to complex actuation combined with twisting and falling motions arising from spatially controlled internal structures that have not been produced by 2D soft lithography. Furthermore, the actuation of helical PNIPAm−AuNR composite gels was observed. Ultrafast actuation was achieved through very fast temperature jump due to the ultrafast light to heat conversion in AuNRs (ps) and the fast heat transfer to the surrounding water (ns). Also, the increase of the density of AuNRs due to the shrinkage of gels may accelerate the sharp transition. As a consequence, the volume change can be operated at non-equilibrium conditions because of the imparity of heat and mass diffusion rates and heterogeneous shrinking dynamics. We prepared dynamic (500 nm) and static (100 nm) helical PNIPAm−AuNR nanocomposite gels (Figure S15). Low-crosslinked dynamic composite gels show shrinkage within 30 ms laser on and reswelled within 100 ms, while static gels did not change their volume (Figure 5g). These results highlighted the principally huge variability in the structural design and control of the local composition. Recently, bioinspired hydrogel microstructures have been fabricated using multi-photon lithography, which can be actuated using pH changes.[28,36] However, it remains a challenge in controlling the three-dimensional internal structures of thermoresponsive hydrogels due to the lack of resolution, caused by the swelling of the hydrogel layers during printing using the conventional photoresist (NIPAm + Bis). To overcome this problem, we have designed a photoresist based on multifunctional PNIPAm macrocrosslinkers, which allows for the fabrication of three-dimensionally anisotropic microstructures with a submicron resolution by tuning the printing density through the program of writing distance. The approach may further contribute to the development of functional soft materials that undergoes complex three-dimensional actuation.

CONCLUSIONS

In summary, we describe the fabrication of stimuli-responsive nanocomposite gel actuators with a defined 3D geometry and programmed printing density by MPL and their ultrafast, reversible shape morphing through plasmonic heating. The newly synthesized PNIPAm macrocrosslinker substantially enhanced the writing efficiency and the resolution of MPL, allowing for 3D fabrication of dynamic−static bilayer helices of PNIPAm−AuNR nanocomposite gels. The programmed printing density served as a driving force to induce complex shape transformation. Light-driven manipulation with AuNRs performed ultrafast, reversible shape morphing based on body deformation. This versatile method can be used for any photoreactive soft material and offers nearly unlimited freedom in the design of the structures and rational engineering of the stress for complex modes of motion.[37] Dynamic control of large amplitude of actuation through plasmonic heating offer the feasibility to develop an adaptive micro-optomechanical system for a tunable switching system, a microfluidic device to mix, sort, and circulate fluids, an artificial muscle, and a microswimmer.

EXPERIMENTAL METHODS

Materials. Tetracholorauric(III) acid trihydrate ($HAuCl_4 \cdot 3H_2O$, >99.9%), silver nitrate ($AgNO_3$, 99.9999%), cetyltrimethylammonium bromide (CTAB, >99%), L-ascorbic acid (reagent grade), sodium borohydride ($NaBH_4$, >99%), carbon disulfide (CS_2, >99%), 1-propanethiol (99%), triethylamine (Et_3N, >99%), diethyl-2,5-dibromohexanedioate (97%), pentaerythritol-tetrakis[2-(dodecylthiocarbonothioylthio)-2-methylpropionate] (TetraDDMAT, 98%), dimethylphenylphosphin (DMPP, 99%), octylamine (99%), tetrahydrofuran (THF, dry, >99.9%), chloroform (p.a., >99%), dichloromethane (DCM, dry, >99%), *N*,*N*′-methylenebis-acrylamide (Bis, 98%), and 3-(trimethoxysilyl)propyl acrylate were purchased from Sigma-Aldrich and used as received. *N*-Isopropylacrylamide (NIPAm, 97%) was purchased from Sigma-Aldrich and recrystallized from hexane and stored under nitrogen in a fridge until needed. 2,2′-Azobis(2-methylpropionitrile) (AIBN, 98%) was purchased from Sigma-Aldrich and recrystallized from MeOH and stored in the fridge until needed. Allyl methacrylate (ALMA, 98%) was purchased from Sigma-Aldrich and passed through a short, neutral Al_2O_3 column prior to use. Thiol-functional poly(ethylene glycol) (HS-PEG-OH, 3 kDa) was purchased from Iris Biotech and stored under nitrogen in the freezer. For the gold nanorod synthesis, we used deionized water (18.2 MΩ·cm, PURELAB Plus, Veolia, U.K.). The photoinitiator, Irgacure 819, was purchased from BASF (Germany). Methacryloxyethyl thiocarbamoyl rhodamine B was purchased from Polysciences, Inc.

Synthesis of the Bifunctional RAFT Agent. The bifunctional, trithiocarbonate RAFT agent was synthesized as reported using 1-propanethiol and diethyl-2,5-dibromohexanedioate as organic substrates.[38] To an ice-cold solution of CS_2 (1.9 mL, 32.095 mmol, 0.97 equiv) and 1-propanethiol (3 mL, 33.088 mmol, 1 equiv) in dry DCM (7.2 mL), Et_3N (4.5 mL, 32.095 mmol, 0.97 equiv) was added dropwise. The so-formed orange solution was then stirred for further 30 min at room temperature. Afterward, diethyl-2,5-dibromohexanedioate (5.89 g, 15.882 mmol, 0.48 equiv) in dry DCM (5 mL) was

https://dx.doi.org/10.1021/acsami.0c02781
ACS Appl. Mater. Interfaces 2020, 12, 12176−12185

added slowly, causing the solution to thicken. The mixture was allowed to stir for further 16 h at room temperature, then diluted with DCM (15 mL), and washed with water (3 × 50 mL). The organic layer was dried over $MgSO_4$, and the solvent was removed under vacuum. The resulting orange oil was dissolved in DCM and passed through a short column of basic Al_2O_3 to yield the bifunctional RAFT agent as an orange oil (yield = 77%). Liquid-state ^1H and ^{13}C NMR spectra were recorded on a Bruker DPX-400 FT NMR spectrometer (400 MHz) and are reported as follows: chemical shift δ (ppm) (multiplicity, coupling constant J (Hz), number of protons, assignment). Chloroform ($CDCl_3$, δ_H = 7.26 ppm, δ_C = 77.0 ppm) was used as an internal standard. Chemical shifts are reported in ppm to the nearest 0.01 ppm for ^1H and ^{13}C NMR spectra. ^1H NMR (400 MHz in $CDCl_3$, δ in ppm, Figure 3): δ = 1.01 (t, J = 7.4 Hz, 6H, $-CH_3$/propyl), δ = 1.26 (td, J = 7.1 Hz, 6H, $-CH_3$/ethyl), δ = 1.73 (q, J = 7.4 Hz, 4H, $-CH_2$/propyl), δ = 2.08 (m, 2.26−1.90, 4H, $-CH_2$/propyl), δ = 3.33 (td, J = 7.3 Hz, 4H, $-CH_2$), δ = 4.18 (td, J = 7.2 Hz, 4H, $-CH_2$/ethyl), δ = 4.84 (d, J = 15.4 Hz, 2H, −CH). ^{13}C NMR (400 MHz in $CDCl_3$, δ in ppm, Figure 4): δ = 13.40 ($-CH_3$/ethyl), δ = 14.05 ($-CH_3$/propyl), δ = 21.39/21.52 ($-CH_2$/propyl), δ = 22.82/22.86 ($-CH_2$), δ = 38.61/39.14 ($-CH_2$/propyl), δ = 52.26/52.29 ($-CH_2$), δ = 61.94 ($-CH_2$/ethyl), δ = 169.88 (−C ═ O, ester), δ = 221.60/221.63 (−S−(C═S)−S−).

Synthesis of Trithiocarbonate-Terminated PNIPAm (PNIPAm(-TTC)$_2$). PNIPAm(-TTC)$_2$ was synthesized by RAFT polymerization. NIPAm (5 g, 44.185 mmol, 100 equiv), a bifunctional RAFT agent (222.2 mg, 0.442 mmol, 1 equiv), and AIBN (7.3 mg, 0.044 mmol, 0.1 equiv) were placed in a nitrogen-flushed Schlenk flask and dissolved in dry THF (16 mL). The solution was at least 4 times degassed by freeze−pump−thaw cycles. Afterward, the Schlenk flask was purged with nitrogen and immersed in an oil bath at 70 °C. The reaction was allowed to run overnight (16 h), then cooled, exposed to air, and diluted with acetone to stop the polymerization. The crude product was precipitated into an excess of cold diethyl ether, filtered, and dialyzed in acetone for at least two days to yield PNIPAm(-TTC)$_2$ as a yellow solid (yield = 52%).

Synthesis of Trithiocarbonate-Terminated PNIPAm (PNIPAm(-TTC)$_3$). PNIPAm(-TTC)$_3$ was synthesized by RAFT polymerization using a trifunctional RAFT agent. NIPAm (5 g, 44.185 mmol, 100 equiv), TrisDDMAT (512.7 mg, 0.442 mmol, 1 equiv), and AIBN (7.3 mg, 0.044 mmol, 0.1 equiv) were placed in a nitrogen-flushed Schlenk flask and dissolved in dry THF (16 mL). The solution was at least 4 times degassed by freeze−pump−thaw cycles. Afterward, the Schlenk flask was purged with nitrogen and immersed in an oil bath at 70 °C. The reaction was allowed to run overnight (16 h), then cooled, exposed to air, and diluted with acetone to stop the polymerization. The crude product was precipitated into an excess of cold diethyl ether, filtered, and dialyzed in acetone for at least 2 days to yield PNIPAm(-TTC)$_3$ as a yellow solid (yield = 61%).

Synthesis of Trithiocarbonate-Terminated PNIPAm (PNIPAm(-TTC)$_4$). PNIPAm(-TTC)$_4$ was synthesized by RAFT polymerization using a tetrafunctional RAFT agent. NIPAm (5 g, 44.185 mmol, 100 equiv), TetraDDMAT (673 mg, 0.442 mmol, 1 equiv), and AIBN (7.2 mg, 0.044 mmol, 0.1 equiv) were placed in a nitrogen-flushed Schlenk flask and dissolved in dry THF (16 mL). The solution was degassed 4 times by freeze−pump−thaw cycles. Afterward, the Schlenk flask was purged with nitrogen and immersed in an oil bath at 70 °C. The reaction was allowed to run overnight (16 h), then cooled, exposed to air, and diluted with acetone to stop the polymerization. The crude product was precipitated into an excess of cold diethyl ether, filtrated, and dialyzed in acetone for three days to yield PNIPAm(-TTC)$_4$ as a dark yellow solid (yield = 55%).

Synthesis of PNIPAm(-allyl)$_2$. The postmodification of PNIPAm(-TTC)$_2$ was done as reported elsewhere,[39] with slight modifications. PNIPAm(-TTC)$_2$ (2.5 g, 0.168 mmol, 1 equiv) was dissolved in dry DCM (11.5 mL) at 50 °C in a nitrogen-flushed flask. Successively, ALMA (1.345 mL, 10 mmol, 60 equiv), DMPP (20.5 μL, 0.144 mmol, 0.9 equiv), and octylamine (2.48 mL, 15 mmol, 89 equiv) were added and the mixture was degassed (3 times) via freeze−pump−thaw cycles. The reaction was allowed to run overnight (16 h). Afterward, the crude product was precipitated into an excess cold diethyl ether, filtrated, and dialyzed in acetone and MeOH for four days to yield PNIPAm(-allyl)$_2$ as a beige solid (yield = 80%).

Synthesis of PNIPAm(-allyl)$_3$. The synthesis of PNIPAm(-allyl)$_3$ was similar to that for PNIPAm(-allyl)$_2$. Briefly, PNIPAm(-TTC)$_3$ (1.5 g, 0.114 mmol, 1 equiv) was dissolved in dry DCM (13.5 mL). Successively, ALMA (915 μL, 6.818 mmol, 60 equiv), DMPP (15 μL, 0.103 mmol, 0.9 equiv), and octylamine (1.68 mL, 10.146 mmol, 89 equiv) were added under nitrogen. The reaction mixture was degassed (3 times) via freeze−pump−thaw cycles and then stirred overnight (18 h) at room temperature. The crude product was precipitated into an excess of cold diethyl ether, filtered, and dialyzed in acetone for at least 3 days to yield PNIPAm(-allyl)$_3$ as a beige solid (yield = 70%).

Synthesis of PNIPAm(-allyl)$_4$. The synthesis of PNIPAm(-allyl)$_4$ was similar to that for PNIPAm(-allyl)$_2$. Briefly, PNIPAm(-TTC)$_4$ (2 g, 0.201 mmol, 1 equiv) was dissolved in dry DCM (13.5 mL). Successively, ALMA (1.62 mL, 12.054 mmol, 60 equiv), DMPP (26 μL, 0.181 mmol, 0.9 equiv), and octylamine (2.95 mL, 17.889 mmol, 89 equiv) were added under nitrogen. The reaction mixture was degassed (3 times) via freeze−pump−thaw cycles and then stirred overnight (18 h) at room temperature. The crude product was precipitated into an excess cold diethyl ether, filtered, and dialyzed in acetone for at least 3 days to yield PNIPAm(-allyl)$_4$ as a beige solid (yield = 27%).

Size-Exclusion Chromatography (SEC). Molecular weights ($M_{n,SEC}$ and $M_{w,SEC}$) and molecular weight distributions (M_w/M_n) were determined by size-exclusion chromatography (SEC). SEC analyses were performed with dimethylformamid (DMF) as an eluent. Results were evaluated using PSS WinGPC UniChrom software (version 8.1.1). SEC with DMF (HPLC grade, VWR) as an eluent was performed using an Agilent 1100 system equipped with a dual RI-/Visco detector (ETA-2020, WGE). The eluent contained 1 g·L^{-1} LiBr (≥99%, Sigma-Aldrich). The sample solvent contained traces of distilled water as an internal standard. One precolumn (8 × 50 mm^2) and four GRAM gel columns (8 × 300 mm^2, Polymer Standards Service) were applied at a flow rate of 1.0 mL·min^{-1} at 40 °C. The diameter of the gel particles was measured to be 10 μm, and the nominal pore widths were 30, 100, 1000, and 3000 Å. Calibration was achieved using narrow distributed poly(methyl methacrylate) standards (Polymer Standards Service).

LCST of PNIPAm. LCST of PNIPAm macrocrosslinker was determined by UV−vis spectroscopy (V-630, JASCO). Polymer solutions (0.5−1.5 mg/mL) in ultrapure water were prepared, and the transmittance of each solution was measured at λ = 500 nm in the range of 20−60 °C. The temperature was varied at a speed of 0.5 °C/min with an interval of 30 s, and the measurements were performed every 0.5 °C.

Viscosity Measurement. The viscosity of each gel photoresist was measured using a controlled stress rheometer (DHR-3, TA Instruments) with a 20 mm diameter of plate geometry. The gel photoresists were prepared by dissolving monomers and crosslinkers in the mixture of ethylene glycol and acetone, but the photoinitiator was not added. The photoresist (73 μL) that covered the whole plate geometry was placed on a stage. The measurement was performed in the sweep mode at 25 °C. The angular frequency range used during testing was 0.1−100 rad/s. The values of viscosity shown in Table S2 are the average of values at 100 rad/s obtained from three different measurements.

Synthesis of Gold Nanorods (AuNRs). Gold nanorods (AuNRs) were synthesized by a seed-mediated method according to a previous report.[40] For the seed solution, 0.60 mL of freshly prepared ice-cold 10 mM $NaBH_4$ (99%, Sigma-Aldrich) aqueous solution was added to 4.2 mL of aqueous solution with 200 mM cetyltrimethylammonium bromide (CTAB, 5.0 mL, 99%, Sigma-Aldrich) and 3 mM hydrogen tetrachloroauric(III) acid ($HAuCl_4$, 0.83 mL, Sigma-Aldrich) under vigorous stirring for 2 min. For the growth solution, 200 mM CTAB (150 mL), 50 mM ascorbic acid (3.1 mL, 99%, Sigma-Aldrich), and 8 mM $AgNO_3$ (3.3 mL, 99.99%, Sigma-Aldrich) were added under stirring to 1 mM $HAuCl_4$ (150

https://dx.doi.org/10.1021/acsami.0c02781
ACS Appl. Mater. Interfaces 2020, 12, 12176−12185

mL). The temperature of the growth solution was kept at 25 °C in a water bath. The seed solution (0.875 mL) was injected into the growth solution under vigorous stirring followed by 30 min of stirring and addition of 50 mM ascorbic acid (2.0 mL) at a flow rate of 0.50 mL/h. After 30 min of stirring, the resultant brownish-red solution of AuNRs was centrifuged at 8000 rpm for 40 min in an Eppendorf Centrifuge 5810. The supernatant containing excess surfactant was discarded, and the precipitated AuNRs were collected and resuspended in water with a final volume of ca. 20 mL. After the last centrifugation, the sedimented gold-containing fraction was collected as a concentrated solution of PEGylated AuNRs in DMSO. The modified AuNRs had a longitudinal absorption band maximum at 791 nm (UV−vis spectrum, V-630, JASCO), and an average diameter of 15.4 nm and a length of 60.0 nm, i.e., an aspect ratio of 3.90.

Modification of AuNRs with PNIPAm or PEG. A general procedure for the modification of CTAB-stabilized AuNRs with thiol-functionalized PEG derivates is as follows: as-synthesized AuNR (20 mL) were centrifuged at 6000 rpm for 30 min. The supernatant was removed, and the AuNRs were redispersed in deionized water. A solution of HS-PNIPAm (M_w = 45 kDa) or HS-PEG-OH (M_w = 3 kDa, 32 mg in 4 mL EtOH) was added, and the reaction mixture was sonicated for 30 min at 60 °C and further 3.5 h at 20 °C.[41] Successively, the mixture was extracted 4 times with $CHCl_3$ (∼20 mL), washed by centrifugation (3× 6000 rpm for 30 min at room temperature), and finally redispersed in deionized water to yield AuNR−PNIPAm or −PEG hybrids (20 mL).

Fabrication of PNIPAm Gels by MPL. The photoinitiator (1 wt %) was dissolved in ethylene glycol/acetone (1:1 (*v*/*v*)). *N*-Isopropylacrylamide (40 wt %) (NIPAm, 97%, recrystallized twice in *n*-hexane) and 2 wt % *N*,*N*′-methylenebis-acrylamide (Bis) were added to the solution and incubated overnight. To prepare a photoresist, 20 wt % allyl-functional PNIPAm, 20 wt % NIPAm, and 2 wt % Bis were dissolved in the photoinitiator solution. To label the gels fluorescently, 0.1−0.5 wt % methacryloxyethyl thiocarbamoyl rhodamine B was added. The prepared photoresist was filtrated with a 0.2 μm syringe filter (Whatman) and placed on a coverslip (30 mm in diameter, 0.13−0.16 mm in thickness). The coverslip was preliminary incubated in 1% 3-(trimethoxysilyl)propyl acrylate/acetone solution overnight to coat the glass surface with reactive acrylate, supporting the adhesion of printed materials. The MPL process was performed using a Photonic Professional DLW system (Nanoscribe GmbH, Germany) with an oil immersion 63× objective lens (numerical aperture (NA), 1.4; Zeiss, Germany). A femtosecond laser (emission wavelength, 780 nm; pulse width, 120 fs; and repetition rate, 100 MHz) was employed as a laser source. The bilayered pillar and helix were designed using computer-aided design (CAD) software (AutoCAD, Autodesk), and the structural designs of the neuron and skeletal bone were obtained from NIH 3D Print Exchange. The slicing distance and hatching distance were adjusted in the range from 100 to 500 nm. The laser power and scanning speed were varied from 30 to 100 mW and 1000 to 10 000 $\mu m \cdot s^{-1}$, respectively. The laser beam was applied to the photoresist according to CAD design, and polymerization/crosslinking at the focal point formed PNIPAm gels. The lateral and axial radii were calculated to 150 and 300 nm, respectively (NA, 1.4; refractive index of the photoresist, *n*, 1.48; wavelength of light, 780 nm), according to a previous report.[42] After the writing process, the structures were washed with acetone overnight to remove unreacted photoresist and then immersed in ultrapure water to swell gels. To prevent gels from sticking to a glass substrate, the washing process was carried out in the solvent without drying.

Observation of Laser-Driven Actuation of Gels. We observed the light-driven actuation of MPL gels using AuNRs and NIR laser exposure. MPL gels prepared on a coverslip (3 cm in diameter) were immersed in ultrapure water. AuNRs dispersed in ultrapure water were added to the gel and stirred, and PDMS mold (outer dimension of 15 × 15 mm^2 and inner dimension of 10 × 10 mm^2) with a coverslip was placed on top of the sample to form a chamber. For the observation of actuation, the samples were placed on a Peltier stage for temperature-control mounting on an optical microscope stage (VHZ-100UR, KEYENCE, Japan). NIR laser light (808 nm, 2.5 W, Roithner Lasertechnik) was focused on the center of the field of view with an incident angle of ∼40°. The mean laser intensity was measured as 1.7 W/mm^2 using an optical power meter (PM200, Thorlab). The laser was modulated with 1 ms temporal resolution. A short-pass filter (700 nm, OD 4, Edmund Optics) was used to block and protect the camera from NIR light. Acquired videos were contrast-enhanced and analyzed with the open-source software ImageJ. For fluorescence observation, a confocal laser scanning microscope (CLSM, Leica TCS SPE, Leica, Germany) with laser setup for the actuation of gels (808 nm, 1 W, Roithner Lasertechnik) and a self-built electrical stage was used. The obtained images were analyzed using Leica Application Suite AF Lite (Leica, Germany) and ImageJ. The ultrahigh-resolution field-emission scanning electron microscopy (FESEM) (S-4800 and SU9000, HITACHI, Japan) was used for the observation of gel structure. Samples were treated with 6 nm thickness of gold or carbon sputtering. An accelerating voltage and working distance were set to 5 kV and 10−15 mm, respectively.

Atomic Force Microscopy (AFM). The measurements were performed on a Dimension Icon AFM with a closed loop (Veeco Instruments Inc.; software, Nanoscope 8.15; Bruker Corporation). They were analyzed by Nanoscope Analysis 1.5 software (Bruker Corporation). The measurements were conducted in a customized liquid cell on a heating stage (Dimension Icon Electrochemistry Chuck, Bruker Corporation) with temperature control (Model 335 cryogenic temperature controller, Lake Shore Cryotronics). The glass slide (with gels on it) was placed in the liquid cell, with a 55 μm thick polyimide (PI) foil beneath at the detector side, and the gels were hydrated by adding water. The gels were analyzed at 25 and 35 °C. The temperatures were equilibrated for ca. 90 min. All measurements were performed at the center of the gels. The position was checked by the optical microscope of AFM.

(i) Height image of hydrated gel surfaces: The measurements were recorded in the Peak Force QNM mode with MSNL-10-F (Bruker Corporation) tips with a nominal resonance frequency of 125 kHz in air and a nominal spring constant of 0.6 N/m of the cantilever (tip radius, 2 nm; semiangle of the tip, 23°; and assumed sample Possion's ratio, 0.3). Before images were taken, the tips used were calibrated. The applied force was 1.8 nN at 25 °C and 3.0 nN at 35 °C.

(ii) Force spectroscopy with colloidal AFM probe: Force spectroscopy measurements were conducted with CP-PNPS−SiO-A-5 (sQUBE) probes with a nominal resonance frequency of 67 kHz in air and a nominal spring constant of 0.32 N/m of the cantilever (sphere diameter, 2 μm; sphere material, SiO_2; and assumed sample Possion's ratio, 0.3). The probe was activated under oxygen flow with UV radiation for 15 min before usage. After calibration of the AFM tip, force−distance curves were obtained. A force of 5 nN was applied. The curves were baseline-corrected (first-order) and fitted to the Hertzian model by Nanoscope Analysis 1.5 Software (Bruker Corporation) after the contact point to obtain Young's modulus. Measurements were taken at three different positions (positions were shifted by 130 nm in the *x*-direction). At every position, 20 measurements were performed. Extracted Young's moduli were averaged for all measurements on one gel at both temperatures. The different measurements at the same position match reasonably well, indicating that the gels are not plastically deformed during the measurement.

(iii) Force spectroscopy with sharp AFM tip: Force spectroscopy measurements were conducted with HQ:NSC36/Cr-Au BS-B (MikroMasch) tips with a nominal resonance frequency of 130 kHz in air and a nominal spring constant of 2 N/m of the cantilever (probe radius, 8 nm; semiangle of the tip, 18°; and assumed sample Possion's ratio, 0.3). After calibration of the AFM tip, force−distance curves were received. A force of 5 nN was applied. The curves were baseline-corrected (first-order) and fitted to the Sneddon model by Nanoscope Analysis 1.5

https://dx.doi.org/10.1021/acsami.0c02781
ACS Appl. Mater. Interfaces 2020, 12, 12176−12185

Software (Bruker Corporation) after the contact point to obtain Young's modulus. Measurements were taken at two different positions (positions were shifted by 130 nm in the *x*-direction). At every position, 15 measurements were performed. Extracted Young's moduli were averaged for all measurements on one gel at both temperatures. The different measurements at the same position match reasonably well, indicating that the gels are not plastically deformed during the measurement.

Tip calibration: To calibrate the AFM tips, force spectroscopy measurements on the solid substrate were conducted. Out of the slope of the deflection−distance−curves (after the contact point), the cantilever sensitivity was determined. The tip was withdrawn from the surface by 400 μm, and the thermal noise was measured by the thermal tune of Nanoscope 8.15 software. The temperature and the average displacement of the cantilever due to thermal noise give rise to the cantilever spring constant. The determined sensitivity and spring constant of the used probes are listed in Table S3.

Transfer of Microgels. The release of the microgels from the mold was carried out by peeling them off with the help of etching using hydrogen fluoride (HF). HF (1%) was added to dried PNIPAm gels prepared on a coverslip of 3 cm diameter. After a few hours, HF was evaporated and PDMS film (500 μm Sylgard 184, Dow Corning) square frames were cut with an outer dimension of 15 × 15 mm^2 and an inner dimension of 10 × 10 mm^2 and placed on the coverslip. Then, ultrapure water was added to the inner part to swell and harvest gels and the PDMS frame was covered with a coverslip.

■ ASSOCIATED CONTENT

Supporting Information

The Supporting Information is available free of charge at https://pubs.acs.org/doi/10.1021/acsami.0c02781.

NMR and SEC results of the PNIPAm macrocrosslinker; LCST measurement of the PNIPAm polymer and macrocrosslinker; TEM images and UV−vis spectra of AuNRs with ARs of 2.5 and 4.4; force−distance curve obtained by a colloidal probe; and shape transformation of bilayer gels composed of a dynamic layer and a static layer with a distance in between (PDF)

■ AUTHOR INFORMATION

Corresponding Author

Martin Möller − *DWI—Leibniz-Institute for Interactive Materials D-52056 Aachen, Germany;* orcid.org/0000-0002-5955-4185; Email: moeller@dwi.rwth-aachen.de

Authors

Akihiro Nishiguchi − *DWI—Leibniz-Institute for Interactive Materials D-52056 Aachen, Germany;* orcid.org/0000-0002-3160-6385

Hang Zhang − *DWI—Leibniz-Institute for Interactive Materials D-52056 Aachen, Germany;* orcid.org/0000-0003-4949-3371

Sjören Schweizerhof − *DWI—Leibniz-Institute for Interactive Materials D-52056 Aachen, Germany*

Marie Friederike Schulte − *DWI—Leibniz-Institute for Interactive Materials D-52056 Aachen, Germany;* orcid.org/0000-0002-9411-242X

Ahmed Mourran − *DWI—Leibniz-Institute for Interactive Materials D-52056 Aachen, Germany;* orcid.org/0000-0003-1607-5739

Complete contact information is available at: https://pubs.acs.org/10.1021/acsami.0c02781

Author Contributions

A.N. designed and carried out the studies and wrote the paper. H.Z. performed the experiments on light-driven actuation of gels. S.S. synthesized and analyzed allyl-functional PNIPAm macrocrosslinkers and functional AuNRs. M.F.S. performed AFM experiments. A.M. helped supervise the project and provided intellectual contibution. A.M. and M.M. developed light-responsive PNIPAm gels with incorporated AuNRs. M.M. supervised the project and edited the paper. The manuscript was written through the contributions of all authors. All authors have given approval to the final version of the manuscript.

Notes

The authors declare no competing financial interest.

■ ACKNOWLEDGMENTS

This work was supported by the German Science Foundation (DFG) within the priority program Microswimmers—From Single Particle Motion to Collective Behaviour (SPP 1726) and in the framework of the SFB 985 A7 project. This work was performed in part at the Center for Chemical Polymer Technology, supported by the EU and the state of North Rhine-Westphalia (Grant No. EFRE 30 00 883 02). M.M. acknowledges support from the ERC Advanced Grant 695716. The authors also thank Dr R. Vinokur for the laser setup.

■ REFERENCES

(1) Naleway, S. E.; Porter, M. M.; McKittrick, J.; Meyers, M. A. Structural Design Elements in Biological Materials: Application to Bioinspiration. *Adv. Mater.* **2015**, *27*, 5455−5476.

(2) Fratzl, P.; Burgert, I. Actuation Systems in Plants as Prototypes for Bioinspired Devices. *Philos. Trans. R. Soc., A* **2009**, *6*, 1541−1557.

(3) Smela, E.; Inganas, O.; Lundstrom, I. Controlled Folding of Micrometer-Size Structures. *Science* **1995**, *268*, 1735−1738.

(4) Tokarev, I.; Minko, S. Multiresponsive, Hierarchically Structured Membranes: New, Challenging, Biomimetic Materials for Biosensors, Controlled Release, Biochemical Gates, and Nanoreactors. *Adv. Mater.* **2009**, *21*, 241−247.

(5) Kim, Y. S.; Liu, M.; Ishida, Y.; Ebina, Y.; Osada, M.; Sasaki, T.; Hikima, T.; Takata, M.; Aida, T. Thermoresponsive Actuation Enabled by Permittivity Switching in an Electrostatically Anisotropic Hydrogel. *Nat. Mater.* **2015**, *14*, 1002.

(6) Ikegami, T.; Kageyama, Y.; Obara, K.; Takeda, S. Dissipative and Autonomous Square-Wave Self-Oscillation of a Macroscopic Hybrid Self-Assembly under Continuous Light Irradiation. *Angew. Chem., Int. Ed.* **2016**, *55*, 8239−8243.

(7) Behl, M.; Razzaq, M. Y.; Lendlein, A. Multifunctional Shape-Memory Polymers. *Adv. Mater.* **2010**, *22*, 3388−3410.

(8) He, X.; Aizenberg, M.; Kuksenok, O.; Zarzar, L. D.; Shastri, A.; Balazs, A. C.; Aizenberg, J. Synthetic Homeostatic Materials with Chemo-Mechano-Chemical Self-Regulation. *Nature* **2012**, *487*, 214−218.

(9) Wehner, M.; Truby, R. L.; Fitzgerald, D. J.; Mosadegh, B.; Whitesides, G. M.; Lewis, J. A.; Wood, R. J. An Integrated Design and Fabrication Strategy for Entirely Soft, Autonomous Robots. *Nature* **2016**, *536*, 451−455.

(10) Mourran, A.; Zhang, H.; Vinokur, R.; Möller, M. Soft Microrobots Employing Nonequilibrium Actuation via Plasmonic Heating. *Adv. Mater.* **2017**, *29*, No. 1604825.

(11) Geryak, R.; Tsukruk, V. V. Reconfigurable and Actuating Structures from Soft Materials. *Soft Matter* **2014**, *10*, 1246−1263.

(12) Ionov, L. Biomimetic 3D Self-Assembling Biomicroconstructs by Spontaneous Deformation of Thin Polymer Films. *J. Mater. Chem.* **2012**, *22*, 19366−19375.

(13) Kim, J.; Hanna, J. A.; Byun, M.; Santangelo, C. D.; Hayward, R. C. Designing Responsive Buckled Surfaces by Halftone Gel Lithography. *Science* **2012**, *335*, 1201−1205.
(14) Wu, Z. L.; Moshe, M.; Greener, J.; Therien-Aubin, H.; Nie, Z.; Sharon, E.; Kumacheva, E. Three-Dimensional Shape Transformations of Hydrogel Sheets Induced by Small-Scale Modulation of Internal Stresses. *Nat. Commun.* **2013**, *4*, No. 1586.
(15) Jamal, M.; Zarafshar, A. M.; Gracias, D. H. Differentially Photo-Crosslinked Polymers Enable Self-Assembling Microfluidics. *Nat. Commun.* **2011**, *2*, No. 527.
(16) Erb, R. M.; Sander, J. S.; Grisch, R.; Studart, A. E. R. Self-Shaping Composites with Programmable Bioinspired Microstructures. *Nat. Commun.* **2013**, *4*, No. 1712.
(17) Skotheim, J. M.; Mahadevan, L. Physical Limits and Design Principles for Plant and Fungal Movements. *Science* **2005**, *308*, 1308−1310.
(18) Ge, Q.; Dunn, C. K.; Qi, H. J.; Dunn, M. L. Active Origami by 4D Printing. *Smart Mater. Struct.* **2014**, *23*, No. 094007.
(19) Gladman, A. S.; Matsumoto, E. A.; Nuzzo, R. G.; Mahadevan, L.; Lewis, J. A. Biomimetic 4D Printing. *Nat. Mater.* **2016**, *15*, 413−418.
(20) Naficy, S.; Gately, R.; Gorkin, R., III; Xin, H.; Spinks, G. M. 4D Printing of Reversible Shape Morphing Hydrogel Structures. *Macromol. Mater. Eng.* **2017**, *302*, No. 1600212.
(21) Zhang, Y. L.; Chen, Q. D.; Xia, H.; Sun, H. B. Designable 3D Nanofabrication by Femtosecond Laser Direct Writing. *Nano Today* **2010**, *5*, 435−448.
(22) Maruo, S.; Nakamura, O.; Kawata, S. Three-Dimensional Microfabrication with Two-Photon-Absorbed Photopolymerization. *Opt. Lett.* **1997**, *22*, 132−134.
(23) Wong, S.; Deubel, M.; Pérez-Willard, F.; John, S.; Ozin, G. A.; Wegener, M.; von Freymann, G. Direct Laser Writing of Three-Dimensional Photonic Crystals with a Complete Photonic Bandgap in Chalcogenide Glasses. *Adv. Mater.* **2006**, *18*, 265−269.
(24) Campagnola, P. J.; Delguidice, D. M.; Epling, G. A.; Hoffacker, K. D.; Howell, A. R.; Pitts, J. D.; Goodman, S. L. 3-Dimensional Submicron Polymerization of Acrylamide by Multiphoton Excitation of Xanthene Dyes. *Macromolecules* **2000**, *33*, 1511−1513.
(25) Nishiguchi, A.; Mourran, A.; Zhang, H.; Möller, M. In-gel direct laser writing for 3D-designed hydrogel composites that undergo complex self-shaping. *Adv. Sci.* **2018**, *5*, No. 1700038.
(26) Kaehr, B.; Shear, J. B. Multiphoton Fabrication of Chemically Responsive Protein Hydrogels for Microactuation. *Proc. Natl. Acad. Sci. U.S.A.* **2008**, *105*, 8850−8854.
(27) Zarzar, L. D.; Kim, P.; Kolle, M.; Brinker, C. J.; Aizenberg, J.; Kaehr, B. Direct Writing and Actuation of Three-Dimensionally Patterned Hydrogel Pads on Micropillar Supports. *Angew. Chem., Int. Ed.* **2011**, *50*, 9356−9360.
(28) Lee, M. R.; Phang, I. Y.; Cui, Y.; Lee, Y. H.; Ling, X. Y. Shape-Shifting 3D Protein Microstructures with Programmable Directionality via Quantitative Nanoscale Stiffness Modulation. *Small* **2015**, *11*, 740−748.
(29) Han, D. D.; Zhang, Y. L.; Ma, J. N.; Liu, Y. Q.; Han, B.; Sun, H. B. Light-Mediated Manufacture and Manipulation of Actuators. *Adv. Mater.* **2016**, *28*, 8328−8343.
(30) Hirokawa, Y.; Tanaka, T. Volume Phase Transition in a Nonionic Gel. *J. Chem. Phys.* **1984**, *81*, 6379−6380.
(31) Anseth, K. S.; Kline, L. M.; Walker, T. A.; Anderson, K. J.; Bowman, C. N. Reaction Kinetics and Volume Relaxation during Polymerizations of Multiethylene Glycol Dimethacrylates. *Macromolecules* **1995**, *28*, 2491−2499.
(32) Schmidt, S.; Zeiser, M.; Hellweg, T.; Duschl, C.; Fery, A.; Möhwald, H. Adhesion and Mechanical Properties of PNIPAm Microgel Films and Their Potential Use as Switchable Cell Culture Substrates. *Adv. Funct. Mater.* **2010**, *20*, 3235−3243.
(33) Hribar, K. C.; Choi, Y. S.; Ondeck, M.; Engler, A. J.; Chen, S. Digital Plasmonic Patterning for Localized Tuning of Hydrogel Stiffness. *Adv. Funct. Mater.* **2014**, *24*, 4922−4926.
(34) Butt, H. J.; Cappella, B.; Kappl, M. Force Measurements with the Atomic Force Microscope: Technique, Interpretation and Applications. *Surf. Sci. Rep.* **2005**, *59*, 1−152.
(35) Domke, J.; Radmacher, M. Measuring the Elastic Properties of Thin Polymer Films with the Atomic Force Microscope. *Langmuir* **1998**, *14*, 3320−3325.
(36) Hu, Y.; Wang, Z.; Jin, D.; Zhang, C.; Sun, R.; Li, Z.; Hu, K.; Ni, J.; Cai, Z.; Pan, D.; Wang, X.; Zhu, W.; Li, J.; Wu, D.; Zhang, L.; Chu, J. Botanical-Inspired 4D Printing of Hydrogel at the Microscale. *Adv. Funct. Mater.* **2020**, *30*, No. 1907377.
(37) Turcaud, S.; Guiducci, L.; Fratzl, P.; Bréchet, Y. J. M.; Dunlop, J. W. C. An Excursion into the Design Space of Biomimetic Architectured Biphasic Actuators. *Int. J. Mater. Res.* **2011**, *102*, 607−612.
(38) Bivigou-Koumba, A. M.; Kristen, J.; Laschewsky, A.; Müller-Buschbaum, P.; Papadaki, C. M. Synthesis of Symmetrical Triblock Copolymers of Styrene and N-isopropylacrylamide Using Bifunctional Bis(trithiocarbonate)s as RAFT Agents. *Macromol. Chem. Phys.* **2009**, *210*, 565−578.
(39) Yu, B.; Chan, J. W.; Hoyle, C. E.; Lowe, A. B. Sequential Thiol-ene/Thiol-ene and Thiol-ene/Thiol-yne Reactions as a Route to Well-defined Mono and Bis End-Functionalized Poly(N-isopropylacrylamide). *J. Polym. Sci., Part A: Polym. Chem.* **2009**, *47*, 3544−3557.
(40) Bartneck, M.; Keul, H. A.; Singh, S.; Czaja, K.; Bornemann, J.; Bockstaller, M.; Möller, M.; Zwadlo-Klarwasser, G.; Groll, J. Rapid Uptake of Gold Nanorods by Primary Human Blood Phagocytes and Immunomodulatory Effects of Surface Chemistry. *ACS Nano* **2010**, *4*, 3073−3086.
(41) Nikoobakht, B.; El-Sayed, M. A. Preparation and Growth Mechanism of Gold Nanorods (NRs) Using Seed-Mediated Growth Method. *Chem. Mater.* **2003**, *15*, 1957−1962.
(42) Tibbitt, M. W.; Kloxin, A. M.; Dyamenahallic, K. U.; Anseth, K. S. Controlled Two-Photonphotodegradation of PEG Hydrogels to Study and Manipulate Subcellular Interactions on Soft Materials. *Soft Matter* **2010**, *6*, 5100−5108.

https://dx.doi.org/10.1021/acsami.0c02781
ACS Appl. Mater. Interfaces 2020, 12, 12176−12185